ADVANCED FUNCTIONAL MATERIALS
www.afm-journal.de

Check for updates

Understanding the Role of Grain Boundaries on Charge-Carrier and Ion Transport in $Cs_2AgBiBr_6$ Thin Films

Zewei Li, Satyaprasad P. Senanayak, Linjie Dai, Gunnar Kusch, Ravichandran Shivanna, Youcheng Zhang, Dipika Pradhan, Junzhi Ye, Yi-Teng Huang, Henning Sirringhaus, Rachel A. Oliver, Neil C. Greenham, Richard H. Friend, and Robert L. Z. Hoye**

Halide double perovskites have gained significant attention, owing to their composition of low-toxicity elements, stability in air, and recent demonstrations of long charge-carrier lifetimes that can exceed 1 µs. In particular, $Cs_2AgBiBr_6$ is the subject of many investigations in photovoltaic devices. However, the efficiencies of solar cells based on this double perovskite are still far from the theoretical efficiency limit of the material. Here, the role of grain size on the optoelectronic properties of $Cs_2AgBiBr_6$ thin films is investigated. It is shown through cathodoluminescence measurements that grain boundaries are the dominant nonradiative recombination sites. It also demonstrates through field-effect transistor and temperature-dependent transient current measurements that grain boundaries act as the main channels for ion transport. Interestingly, a positive correlation between carrier mobility and temperature is found, which resembles the hopping mechanism often seen in organic semiconductors. These findings explain the discrepancy between the long diffusion lengths >1 µm found in $Cs_2AgBiBr_6$ single crystals versus the limited performance achieved in their thin film counterparts. This work shows that mitigating the impact of grain boundaries will be critical for these double perovskite thin films to reach the performance achievable based on their intrinsic single-crystal properties.

1. Introduction

Inspired by the tremendous success of the lead-halide perovskites, there has been a resurgence of interest in halide elpasolites, or double perovskites, over the past five years.[1–5] Double perovskites have the general formula $A_2B(I)B(III)X_6$, in which A is a monovalent cation (e.g., Cs^+), B(I) and B(III) are monovalent and trivalent metal cations, respectively, and X is a halide anion (e.g., I^-, Br^-, or Cl^-).[1,6,7] Thus, double perovskites substitute the toxic Pb^{2+} cation with two low-toxicity metal cations (e.g., Ag^+ and Bi^{3+}) without compromising the 3D symmetric perovskite crystal structure. Long charge-carrier lifetimes in the microsecond range and improved environmental stability over lead-halide perovskites have been reported for halide double perovskite compounds.[8,9] These promising properties have led to extensive efforts to develop these materials for a wide range of applications, particularly in photovoltaics, radiation detectors, and photocatalysts.[10–12]

However, the best reported power conversion efficiency (PCE) for a planar solar cell device based on any halide double perovskite thin film is only 2.84%.[10] This result was achieved with a $Cs_2AgBiBr_6$ thin film absorber, which is the halide double perovskite that has been investigated the most for photovoltaic applications.[8,13–16] But even considering its large and indirect bandgap of 2.25 eV, the current efficiency record is still three times lower than the spectroscopic limited

Z. Li, L. Dai, R. Shivanna, Y. Zhang, J. Ye, Y.-T. Huang, H. Sirringhaus, N. C. Greenham, R. H. Friend
Cavendish Laboratory
Department of Physics
University of Cambridge
JJ Thomson, Avenue, Cambridge CB3 0HE, UK

S. P. Senanayak, D. Pradhan
Nanoelectronics and Device Physics Lab
School of Physical Sciences
National Institute of Science Education and Research
HBNI, Jatni 752050, India
E-mail: satyaprasad@niser.ac.in

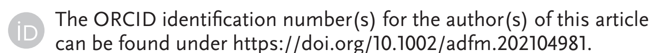
The ORCID identification number(s) for the author(s) of this article can be found under https://doi.org/10.1002/adfm.202104981.

© 2021 The Authors. Advanced Functional Materials published by Wiley-VCH GmbH. This is an open access article under the terms of the Creative Commons Attribution License, which permits use, distribution and reproduction in any medium, provided the original work is properly cited.

DOI: 10.1002/adfm.202104981

G. Kusch, R. A. Oliver
Department of Materials Science and Metallurgy
University of Cambridge
27 Charles Babbage Road, Cambridge CB3 0FS, UK

Y. Zhang
Cambridge Graphene Centre
Department of Engineering
University of Cambridge
9 JJ Thomson Ave, Cambridge CB3 0FA, UK

R. L. Z. Hoye
Department of Materials
Imperial College London
Exhibition Road, London SW7 2AZ, UK
E-mail: r.hoye@imperial.ac.uk

maximum efficiency calculated based on its absorption spectrum.[1] The limited performance, especially the low short-circuit current density, implies a significant impact of defect states, which reduce carrier transport lengths.[10,17–19]

For single crystals, trap densities of 10^{16}–10^{17} cm^{-3} have been reported, and these defects have been attributed to bromide vacancies formed due to surface bromine degassing.[19] Despite the high trap densities, charge-carrier lifetimes exceed 600 ns owing to the shallow nature of the majority of traps.[4,13] Furthermore, in single crystals, mobilities of 11.8 cm^2 V^{-1} s^{-1} (from space charge-limited current density measurements)[11] and diffusion lengths exceeding 1 µm (from stroboscopic scattering microscopy)[20] have been reported, despite trap-limited transport.

Despite these long diffusion lengths in single crystals, carrier transport in the thin films used in photovoltaic devices is significantly lower, with electron diffusion lengths of only 30 nm and mobilities <1 cm^2 V^{-1} s^{-1}.[19] The discrepancy between the 30 nm carrier diffusion length in thin films and the micrometer diffusion length in single crystals is often attributed to fast recombination in surface states due to the accumulation of defects on the surface.[13] It is also suggested that the formation of twin boundaries in single crystals can reduce the charge-carrier lifetime.[15] However, despite their likely importance, an effect that has not been directly accounted for is the impact of grain boundaries on the optoelectronic properties of $Cs_2AgBiBr_6$. Establishing how charge-carriers and ions interact with grain boundaries is essential for understanding the discrepancies between the transport properties of polycrystalline thin films and single crystals, and how the performance of double perovskite thin films could be improved.

Grain boundaries break the periodicity of single crystals and, with few exceptions, lead to an accumulation of dislocations, vacancies and dangling bonds, as well as other structural and point defects, giving rise to defect states in the band gap.[21,22] These localized sub-bandgap states can enhance the nonradiative recombination of photogenerated carriers, and therefore reduce photovoltaic performance.[23] On the other hand, in some cases, the built-in electric field induced by the grain boundary can result in more efficient charge collection.[24,25] Various spatially resolved techniques, such as scanning probe microscopy (Kelvin probe force microscopy, scanning capacitance microscopy, conductive-probe atomic force microscopy), laser-beam-induced current microscopy, and cathodoluminescence (CL), have been used to compare the band bending, charge collection and recombination at the boundaries versus interiors of grains in polycrystalline solar cells.[22,26,27]

In this work, we investigate the role of grain boundary density by synthesizing and characterizing $Cs_2AgBiBr_6$ thin films with three different grain sizes. Through transient absorption spectroscopy (TAS), we measured how the grain boundary density affects charge-carrier lifetimes. We used CL mapping to compare the nonradiative recombination rate at grain boundaries versus in the bulk of the grains. To understand the role of grain boundaries on carrier transport, we developed thin film transistors (TFTs) using $Cs_2AgBiBr_6$ in the active channel and measured the temperature dependence of the field-effect mobility. This also represents the first report of the field-effect transistor (FET) performance in this material, and one of the handful reports of p-type field-effect behavior among halide perovskites, especially in structurally 3D perovskites. Through these field-effect transistor measurements, as well as temperature-dependent transient current measurements, we provide a direct correlation between charge-carrier transport and ionic transport via grain boundaries.

2. Results and Discussion

2.1. Phase Purity and Grain Size

$Cs_2AgBiBr_6$ thin films were synthesized by solution processing, as detailed in the Experimental Section. To tune the grain size, the concentration of the precursor solution was adjusted to 0.3, 0.4, and 0.5 mol L^{-1} (M). The phase purity of the films was determined through X-ray diffraction (XRD) measurements (**Figure 1**a). The larger peak intensity for the higher concentration films was due to increased film thickness. Only peaks due to the double perovskite phase were present. In particular, the common impurity peak at 8.95° for $Cs_3Bi_2Br_9$ was absent,[3] and we have previously verified that any phase impurities in the film would be detectable by 1D linescan measurements.[28] The full width at half maximum (FWHM) of the XRD peaks decreased for films grown from higher concentration solutions, implying an increase in crystallite size (Figure 1b,c). The crystallite sizes obtained by fitting the XRD peaks were 72 ± 7 nm (0.3 M), 98 ± 7 nm (0.4 M), and 113 ± 3 nm (0.5 M), as shown in Figure 1c (details in the Supporting Information). Consistent with these XRD results, we found from top-down scanning electron microscopy (SEM) images that the apparent grain size increased from 160 ± 10 nm (0.3 M) to 200 ± 20 nm (0.4 M) and 370 ± 40 nm (0.5 M), as shown in Figure 1d–f. The measured apparent grain sizes are slightly larger than the film thicknesses from profilometry, which are 118 ± 4 nm (0.3 M), 160 ± 3 nm (0.4 M), and 242 ± 6 nm (0.5 M). From cross-sectional SEM images (Figure S1, Supporting Information), there is one grain throughout the thickness of the film, which is consistent with the typical growth of halide perovskites from solution.[29] The differences between the crystallite and microfeature sizes found from XRD versus SEM measurements may have been due to the microfeatures in SEM being composed of several crystallites, because of a variation in grain size and the narrower XRD peaks from the larger grains being hidden behind the broader peaks from the smaller grains, or because the XRD peaks were broadened due to other factors, such as stacking faults. To avoid ambiguity, we hereafter refer to the films based on the concentration of the precursor solution they were deposited from (rather than their XRD or SEM grain/microfeature size).

2.2. Charge-Carrier Recombination

In **Figure 2**a, we show the absorbance of the films measured by ultraviolet–visible (UV–vis) spectrophotometry. As expected, the absorbance increased with increasing film thickness. In photovoltaic devices, carrier extraction depends on the drift and diffusion lengths, and the two key components in this regard are the charge-carrier lifetime and mobility. Transient absorption spectroscopy (TAS) was used to measure the charge-carrier lifetime of the films, which were excited with a 355 nm wavelength

© 2021 The Authors. Advanced Functional Materials published by Wiley-VCH GmbH

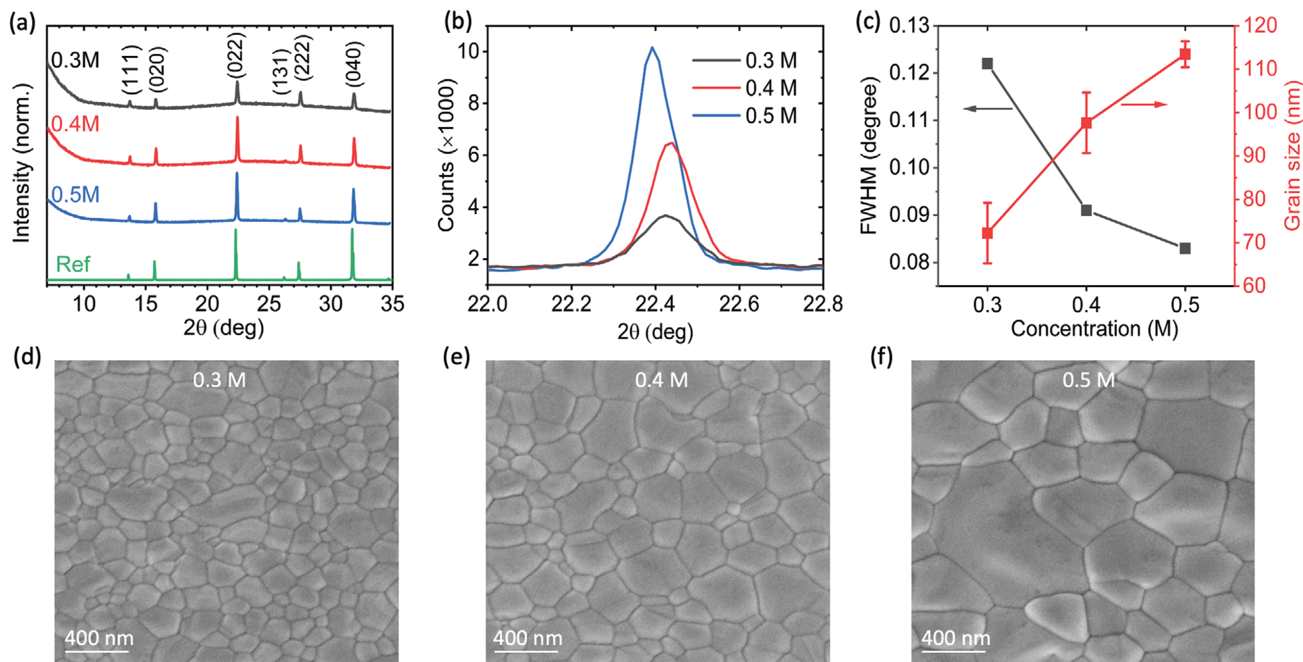

Figure 1. a) XRD patterns of $Cs_2AgBiBr_6$ films grown from three different precursor concentrations. The reference pattern is calculated from its crystallographic information file, obtained from ref. [3]. b) Close-up of the (022) peak for the $Cs_2AgBiBr_6$ films from (a). c) Comparison of the full width at half maximum (FWHM) of the (022) peak with the grain size calculated from the Scherrer equation (Table S1, Supporting Information). Scanning electron microscopy images of $Cs_2AgBiBr_6$ thin films grown from precursor solutions with concentrations of d) 0.3 M, e) 0.4 M, and f) 0.5 M. The thickness of the 0.3, 0.4, and 0.5 M thin films were 118 ± 4, 160 ± 3 nm, and 242 ± 6 nm, respectively.

pump laser incident on the top surface of the films. We found two ground state bleach (GSB) and two photo-induced absorption (PIA) features in the TAS spectra (Figure 2b). The GSB peak below 380 nm wavelength is ascribed to a localized state well above the conduction band minimum.[30,31] However, the explanation for the GSB peak at ≈440 nm wavelength has been the subject of controversy. Some previous studies attributed this peak to a resonant exciton associated with the first direct transition of $Cs_2AgBiBr_6$.[15,31,32] There are also calculations showing that this peak could be due to a narrow distribution of states with a direct transition above the indirect band-edges and which have high oscillator strength.[28] Consistent with the GSB peak at 440 nm being due to excitons, the two PIA signals on either side of the main GSB peak (440 nm) are attributed to the broadening of the direct exciton transition introduced by carrier-exciton scattering.[31,33] The origins of these GSB and PIA peaks are beyond the scope of this work, and we do not discuss them further here. However, in either cases, the decay of carriers from states at the first direct transition or the decay of excitons provide important information on nonradiative recombination processes, and a comparison can be made between different samples of the nonradiative recombination rate based on these GSB kinetics. We did not observe any GSB at wavelengths longer than 550 nm. We attribute this to a

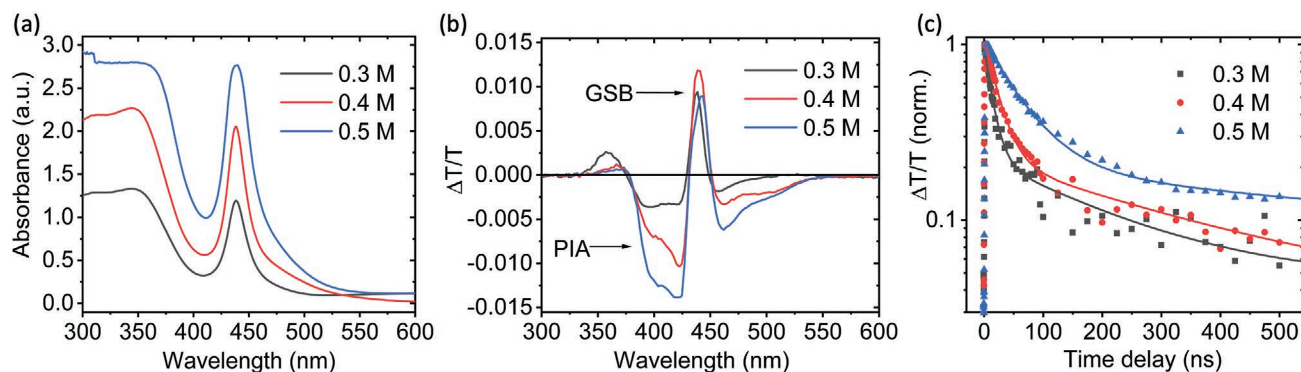

Figure 2. Absorption measurements and kinetics of $Cs_2AgBiBr_6$ thin films grown from three different precursor solution concentrations. a) Steady-state absorbance of the thin films grown on glass. b) $\Delta T/T$ spectra for the integrated time range of 1–10 ns. c) Normalized kinetics of the ground state bleach (GSB). The $\Delta T/T$ values were integrated over the wavelength range of 437–442 nm. The excitation wavelength was 355 nm for laser pulses with a pulse length less than 1 ns at a repetition rate of 1 kHz and fluence of 50 µJ cm^{-2} $pulse^{-1}$.

© 2021 The Authors. Advanced Functional Materials published by Wiley-VCH GmbH

combination of two effects: i) the weak absorption at the indirect bandgap (as seen in the steady-state spectra in Figure 2a) and ii) the neighboring PIA peak covering any weak GSB that may exist here.

Irrespective of the intrinsic nature of the sharp bleach peak at ≈440 nm wavelength, it clearly shows the repopulation of the ground state with time after the absorption of the femtosecond pump laser. We integrated the GSB over the wavelength range of 437–442 nm to characterize the carrier lifetime because this peak has high intensity and a high signal-to-noise ratio. While the GSB kinetics could be fit with a drift-diffusion model to determine the charge-carrier lifetime and surface recombination velocity,[29] this requires a large number of variables to be fit to a single kinetics curve, and it cannot be guaranteed that the fit obtained is the global minimum rather than one of the local minima. We therefore fit the data with a bi-exponential function, which, while not necessarily being physically-relevant, provides a numerical comparison between the GSB kinetics of different samples (Figure 2c). For the 0.3, 0.4, and 0.5 M films, the time constants of the short-lived components of the bi-exponential function are 14 ± 1, 22 ± 1, and 59 ± 1 ns, respectively, and long-lived components are 210 ± 30, 330 ± 30, and 1000 ± 100 ns, respectively (Table S2, Supporting Information). Due to the indirect nature of its bandgap and thus the low photoluminescence quantum efficiency (PLQE), most carriers recombine nonradiatively.[8] We attribute the fast component to the trapping of one carrier and the slow component to the subsequent nonradiative recombination process, which would happen if traps are shallow.[34]

An alternative explanation for the change in GSB kinetics is the difference in film thicknesses across the films from 120 nm (0.3 M) to 240 nm (0.5 M) leading to different degrees of contribution from surface recombination to the overall GSB kinetics measured. However, the absorption coefficient of the film at the TA excitation wavelength (355 nm) is 2×10^5 cm^{-1}, and therefore the absorption depth is 50 nm. The out-of-plane electron diffusion length in $Cs_2AgBiBr_6$ thin film is reported to be around 20–30 nm.[19] Carriers are therefore unlikely to diffuse to the back surface and recombine rapidly there. In addition, when we excited the films from the back (i.e., glass substrate side), we found that the kinetics had the same decay profile (as compared to excitation from the film side), and the change in kinetics with film thickness follows the same trend (Figure S2, Supporting Information). Overall, these analyses show that the change in GSB kinetics are due to changes in the bulk carrier lifetime of the films as the grain size changed with film thickness.

The TAS measurements performed above and by others only give carrier kinetics spatially averaged over the measurement spot, which has a diameter of 1.6 mm. To move beyond spatially-averaged metrics and directly compare the optoelectronic properties of the grain boundary and interior, we used CL hyperspectral mapping, which takes place inside an SEM and provides spatial resolution beyond the optical limit. CL results from the radiative recombination of excess electrons and holes generated by the incident electron beam (e-beam), with the lateral resolution depending on the beam electron energy (which controls the interaction volume) and the carrier diffusion length. The acceleration voltage used in this study was 3 kV, corresponding to a penetration depth of 67 nm according to Monte Carlo simulations using Monte Carlo Casino (Figure S3, Supporting Information).[35] Thus, the interaction volume size in CL is significantly smaller than in confocal PL,[36] providing sufficient spatial resolution to differentiate between the grain boundary and interior.

We were able to compare the CL intensity of the perovskite peak with the secondary electron (SE) image by fitting a Gaussian function to the halide double perovskite signal in each pixel of the map and extracting the fitted intensity using the HyperSpy Python Library, which is given in ref. [37]. By superimposing the perovskite CL peak intensity map on the SE image, we found a distinct difference between the CL intensity at grain boundaries versus grain interiors. For all three samples, we found that the grain interior shows a much higher CL emission intensity than the grain boundary (**Figure 3**). This observation suggests that grain boundaries act as the main nonradiative recombination sites in the investigated samples. This may be due to disorder or dangling bonds at the grain boundary, but could also be due to the accumulation of point defects adjacent to the grain boundary, and is consistent with

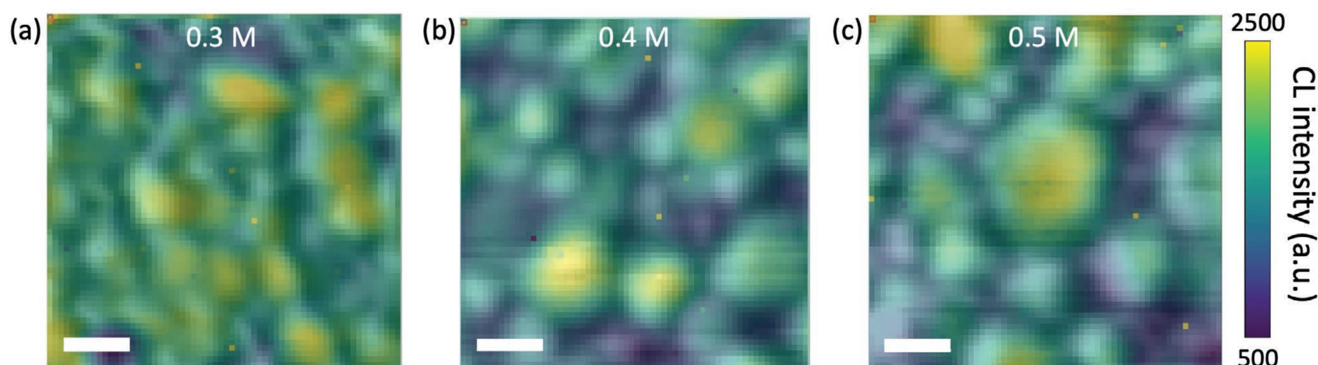

Figure 3. Fitted cathodoluminescence intensity maps overlaid on the secondary electron microscopy images of the $Cs_2AgBiBr_6$ double perovskite thin films grown from precursor solutions with the concentrations a) 0.3 M, b) 0.4 M, and c) 0.5 M. All scale bars are 200 nm. All three measurements were performed with an acceleration energy of 3 keV and a beam current of 500 pA. Note that different acquisition times were used for different CL maps. A comparison of the CL intensity, corrected for the different acquisition times, of the grain interiors between different samples is given in Figure S4 (Supporting Information).

© 2021 The Authors. Advanced Functional Materials published by Wiley-VCH GmbH

the GSB kinetics becoming slower with a reduction in the grain boundary density. The origin of luminescence in CL is attributed to be the same as in PL, that is, due to sub-bandgap state emission.[16] These measurements are consistent with the PL intensity from the film increasing with grain size, as we show in Figure S4a (Supporting Information). We verified that these changes in PL intensity were due to a reduction in the grain boundary density by comparing the CL intensity (corrected for acquisition time, i.e., given in counts s^{-1}) in the interior of the grains and finding there to not be a monotonic trend with grain size (Figure S4b, Supporting Information). These results suggest that nonradiative recombination within each grain depends on the local defect density, whereas the PL intensity, measured on a millimeter scale, is dominated by nonradiative recombination at grain boundaries.

We have additionally measured a series of spectra recorded at the same point to address variations in CL emission intensity with the amount of exposure to the electron beam. Lead-halide perovskites are known to be highly beam sensitive, potentially leading to alterations in both the emission wavelength and emission intensity under the electron beam which could have influenced our measurements. We found that all samples show a degradation in the luminescence intensity with increasing excitation time, but the onset of this degradation was at least an order of magnitude larger than the pixel dwell time used in the hyperspectral images (Figure S5, Supporting Information). It is thus unlikely that our measurements have been strongly affected by these effects. No change in the emission energy with excitation time was observed for any of the samples. We further note that morphology can also influence the CL signal. In troughs, such as grain boundaries, the increased scatter of electrons leads to increased electron–hole pair generation and therefore a larger CL signal.[38,39] But in our case, it is evident from Figure 3 that these morphological effects are negligible compared to the effects of nonradiative recombination, since grain boundaries are consistently darker than the interior of the grains.

2.3. Charge-Carrier and Ion Transport

FETs (bottom gate, bottom contact) were fabricated by spin-coating the specific concentration of perovskite on top of lithographically patterned Au source and drain electrodes. Currently in the broader literature, the demonstration of perovskite FETs has been difficult due to significant ionic defect migration, which screens the gate potential. To the authors' knowledge, this work represents the first report of FETs from halide double perovskites. Interestingly, FETs fabricated from these double perovskites exhibit room temperature (RT) p-type field effect transport (accumulation and switch-on occur for negative gate biases), with current modulation in the range of 10^3 (**Figure 4**a and Figures S6 and S7, Supporting Information). This is consistent with the p-type character of the $Cs_2AgBiBr_6$ films previously found from X-ray photoemission spectroscopy measurements.[8,28] p-type FETs are important for making CMOS complementary inverter circuits but have been generally more difficult to achieve than n-type FETs for perovskite semiconductors.[40] Despite the "anti-clockwise" hysteresis in the device characteristics, it was possible to reliably extract a hole μ_{FET} from the forward scan plot which tend to be a more conservative estimate of mobility. The μ_{FET} values estimated from the linear fits to $I_d^{0.5}$ versus V_g exhibit reliability factors in the range of 55%–79% (Figure S8, Supporting Information), which are comparable to other nonideal perovskite FETs.[41] Devices fabricated with 0.3 M perovskite precursor solution exhibited a room-temperature field effect mobility (μ_{FET}) of 1×10^{-4} cm^2 V^{-1} s^{-1}, which increased by around 6–15 times upon increasing the precursor concentration to 0.5 M. It should be noted that although it was possible to observe field effect modulation at room temperature, the transfer characteristics exhibit features that are non-ideal, and further optimization is essential to achieve near-ideal transistor characteristics. Similarly, the output characteristics measured from these FETs exhibit clear signatures of ionic migration without a clean saturation regime (detailed discussion is provided in Section S4, Supporting Information). The observed nonideal transistor characteristics complicate the understanding of the underlying transport physics. However, we have been able to mitigate the possible factors to an extent such that meaningful $\mu_{FET}(T)$ behavior can be observed (Figure 4b), and the mobilities extracted from the forward and reverse sweeps differ only by 12%. In typical 3D perovskite FETs fabricated from $MAPbI_3$, a negative coefficient of mobility with temperature is observed, since the ionic screening of gate potential decreases with a decrease in temperature.[42] However, in the case of these double-perovskite-based

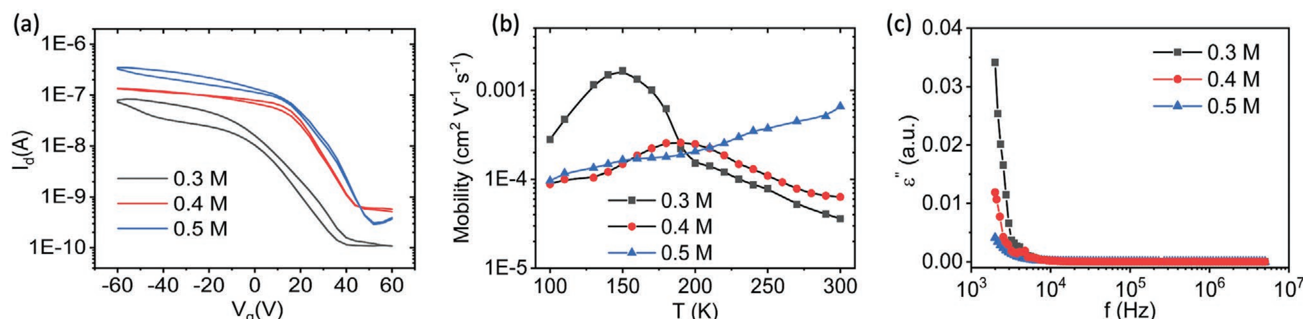

Figure 4. a) Transfer curves of $Cs_2AgBiBr_6$ thin films grown from precursor solutions with 0.3, 0.4, and 0.5 M concentrations. The measurements were conducted on bottom contact bottom gate field-effect transistors at 300 K (FETs with L = 20 µm, W = 1 mm), V_d = −60 V. b) Temperature-dependent FET mobility and c) dielectric loss for $Cs_2AgBiBr_6$ thin films grown from three different concentrations.

© 2021 The Authors. Advanced Functional Materials published by Wiley-VCH GmbH

FETs, we observed a transition from a positive coefficient of mobility to negative coefficient of mobility as temperature increased for devices fabricated with perovskite precursor concentrations of 0.3 and 0.4 M. As the grain size increased, we observed a positive coefficient of field-effect mobility, which is typical of a thermally activated hopping mechanism of transport.[43] These $\mu_{FET}(T)$ trends are indicative of the fact that upon increasing the grain size it is possible to observe a transport regime where the ionic screening of the gate potential can be minimized to an extent such that a hopping mechanism of transport, which is likely intrinsic to the material, is observed.

To verify our proposal that the negative coefficient of mobility in double perovskite films with small- and medium-sized grains in the high temperature regime is due to the stronger screening effect induced by ion motion, we estimated the ionic conductivity in the perovskite films through impedance measurements on perovskite devices with the capacitor structure: ITO/Au/$Cs_2AgBiBr_6$/Au. The dielectric loss spectroscopy measurements showed that perovskite devices fabricated with 0.3 M precursor concentration had a significantly higher ionic conductivity, which then decreased by an order of magnitude as the precursor concentration increased to 0.5 M (Figure 4c).

To further verify if ionic transport increases with grain boundary density, we conducted temperature-dependent transient current measurements. For these measurements, we used hole-only devices due to the aforementioned p-type character of the films. Mobile ions in perovskites with an electric field applied can migrate to the contact layers.[44,45] In a typical $MAPbI_3$ perovskite, when applying a bias, halide anions migrate to the anode (where holes are being injected), while MA^+ cations migrate to the cathode (where electrons are being injected).[46]

We noticed that there is a temporal increase in the hole current density in all three films (**Figure 5**a–c). The increase in current is due to enhanced hole injection by the accumulation of anions at the anode interface,[46] most likely Br^-, as bromide vacancies (V_{Br}) have been calculated to be the lowest formation energy donor defects in $Cs_2AgBiBr_6$.[47] This agrees with calculations showing that V_{Br} has the lowest activation energy for vacancy-assisted diffusion among the four constituent vacancies.[11] In principle, hole transport should also be impeded by the screening effect (accumulation of ions on the gate interface) which will lead to a current decay. However, the enhanced hole injection at the anode interface due to ion migration plays a dominant role, so we mainly observed a slow current rise.[46] It was observed that the stabilized current decreased with higher precursor concentrations (i.e., increased film thickness). The temperature dependence in all three films further confirms that the transient increase in current is due to the drift of mobile ions, which are arrested at lower temperatures. We notice that the transient current has two components: a faster component (exponential rise) and a slower component (nearly linear rise). We attribute the faster component to Br^- motion to the anode followed by facilitated hole injection and the slower component to the drift of other heavy ions (both cation and anion, which is difficult to distinguish). An increase in grain boundary density led to an increase in the exponential growth component of the transient

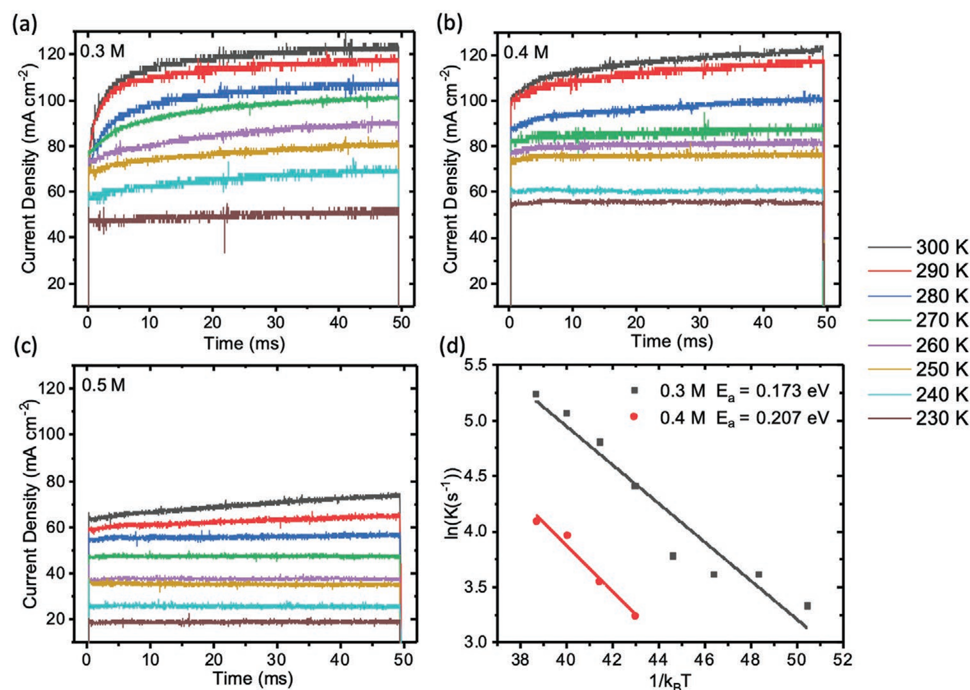

Figure 5. Temperature-dependent transient current measurements of hole-only devices with $Cs_2AgBiBr_6$ thin films deposited from precursor solutions with a) 0.3 M, b) 0.4 M, and c) 0.5 M concentration. The device structure was ITO/NiO_x/$Cs_2AgBiBr_6$/PTAA/Au (pulse voltage = 3.0 V, reference voltage = 0 V, frequency = 4 Hz, and pulse width = 50 ms). d) Arrhenius plots of the temperature dependence of the natural logarithm of K against the inverse of k_BT. Note K in the vertical axis is the decay rate (s^{-1}), as obtained from Equation (2). The activation energy for ion migration (E_a) was extracted by linear fitting.

© 2021 The Authors. Advanced Functional Materials published by Wiley-VCH GmbH

current due to excess Br^- motion. To extract the activation energy of the ion motion, we fit the faster current response with the single-exponential function below

$$J = A\exp\left(-\frac{t}{\tau}\right) + y_0 \quad (1)$$

The fitting parameters are summarized in Tables S3–S5 (Supporting Information). When the temperature is high and the concentration of films low, the model's fit converged. However, at low temperatures and higher concentration films, especially the 0.5 M film, the fittings did not converge. This is due to the heavily impeded exponential growth and the almost linear increase in current (Figure 5c). Therefore, we cannot extract a time constant from low temperatures in the 0.4 M film and all curves in the 0.5 M film.

To extract the ion motion activation energy, we fit the available time constant with the following equation[46]

$$K = \frac{1}{\tau} \propto \sigma = C\exp\left(-\frac{E_a}{k_B T}\right) \quad (2)$$

In Equation (2), K is the rate at which the current increases in the initial faster part of the transient current response, τ is the time constant from Equation (1), σ is ionic conductivity, C is a constant coefficient, E_a is the activation energy for ion migration, k_B is the Boltzmann constant, and T is temperature. To extract the activation energy, we conducted linear fits to $\ln(K)$ versus $(k_B T)^{-1}$ (Figure 5d). The slopes of the linear fit give the negative of the activation energy. Due to the diminished exponential growth component discussed above, we were only able to extract the activation energy for the 0.3 and 0.4 M films (the latter using only the four highest temperature curves). The low temperature data points for the 0.3 M film deviate more from the fitted trend line due to the uncertainties in fitting the nearly-linear initial current transients. The data from the 0.5 M film did not fit to an exponential decay model, and this agrees with an increase in the activation energy barrier for ion migration. The activation energies in the other two films (0.17 ± 0.04 eV for 0.3 M; 0.21 ± 0.05 eV for 0.4 M) are consistent with the analysis that ionic transport through grain boundaries and therefore ionic diffusion is prominent in films grown from lower concentration precursor solutions (with higher densities of grain boundaries). In contrast, $Cs_2AgBiBr_6$ single crystals have been reported to have an activation energy of 0.348 eV,[11] suggesting that ion migration in $Cs_2AgBiBr_6$ single crystals is indeed more difficult. It is noted that while the film thickness changes across the three different samples, the resulting changes in the internal electric field would not influence the values of the activation energy barriers obtained. This is because the activation energy barrier is determined from an Arrhenius plot that depends on the change in time constant with temperature in each film (slope of $\ln(1/\tau)$ against $1/k_B T$), instead of the absolute value of the time constant itself. Another way of looking at this is that the activation energy barrier is primarily affected by the local environment the ions are in,[48,49] and changes in the internal electric field by a factor of two would not influence the mechanism of ion migration. The changes in activation energy would therefore reflect the effects of a change in grain boundary density. Therefore, we conclude that grain boundaries are the main channels for ion movement in $Cs_2AgBiBr_6$ thin films.

Finally, we note that up to now, most works investigating carrier transport in halide double perovskites have used spectroscopy-based techniques, such as time resolved microwave conductivity (TRMC) and time resolved terahertz spectroscopy (TRTS).[13,14,50] By achieving halide double perovskite FETs with reasonable current modulation at room temperature, we provide important insights into the macroscopic carrier transport mechanisms of thin films that account for the effects of point and extended defects. This information is complementary to that obtained from spectroscopy-based methods, which measure the local mobility of photoexcited carriers. Beyond providing insights into the role of grain boundaries on the ion migration dynamics, as discussed above, the FET measurements also show carrier transport to be intrinsically limited by a thermally activated hopping-based mechanism,[51,52] in which the field-effect mobility increases as a function of temperature once the effects of gate screening by ionic defects is minimized (Figure 4b). In contrast, previous TRMC measurements have suggested carrier transport in $Cs_2AgBiBr_6$ and related materials to be band-like, in which mobility decreases with increasing temperature.[13,14] Further work is needed to resolve these differences between local and macroscopic electronic measurements of carrier transport, which could be influenced by the point defects that accumulate at grain boundaries (through direct carrier trapping,[20] or through self-trapping due to the influence of the defects on the interactions between carriers and acoustic phonons),[33,53,54] or due to the inherent energetic disorder in the material. FET measurements of double perovskites could play an important role in shedding light on the underlying mechanisms for this thermally activated hopping behavior.

3. Conclusions

In summary, by tuning the grain size, we achieved a direct evaluation of the effect of grain boundary density on charge-carrier and ion transport in $Cs_2AgBiBr_6$ thin films. We found that grain boundaries are the dominant nonradiative recombination sites and also act as the main channel for ion migration. Furthermore, by developing the first p-type halide double perovskite FET, we gained new insights into carrier transport and ion migration over the bulk film. While previous spectroscopy measurements have suggested band-like transport in $Cs_2AgBiBr_6$, these FET measurements showed carrier transport to be intrinsically limited by a thermally activated hopping mechanism, which helps to explain the low mobilities found in $Cs_2AgBiBr_6$. Taken together, these results reveal grain boundaries to be one of the major causes of the discrepancy between the promising optoelectronic properties reported in single crystals and the more limited performance achieved in $Cs_2AgBiBr_6$ thin films. Our work therefore shows how grain boundaries could mask the true potential of new compounds and the importance of addressing the effects of grain boundaries in the exploration of new compounds in thin film devices to prevent false negatives, which could be achieved using the systematic characterization approach we develop in this work. Addressing the role of defects at grain boundaries, such as through

© 2021 The Authors. Advanced Functional Materials published by Wiley-VCH GmbH

passivation, will be essential for the further development of the halide double perovskite family in efficient thin film devices, including solar cells, photoelectrochemical cells and radiation detectors.

4. Experimental Section

Synthesis of $Cs_2AgBiBr_6$ Thin Films: 1.5 mmol CsBr (99.9%, Sigma Aldrich), 0.75 mmol AgBr (99.998%, Alfa Aesar), and 0.75 mmol $BiBr_3$ (99.998%, Sigma Aldrich) were dissolved in 1.5 mL anhydrous dimethyl sulfoxide (DMSO; 99.9%, Sigma Aldrich) and mixed at 700 rpm at RT inside a N_2 glovebox for an hour to form the 0.5 mol L^{-1} $Cs_2AgBiBr_6$ solution. The solution was then filtered by 0.2 µm PTFE membranes (Sigma Aldrich). 0.5 mL $Cs_2AgSbBr_6$ solution was mixed with 0.125 mL DMSO to form the 0.4 mol L^{-1} $Cs_2AgBiBr_6$ solution. Another 0.5 mL $Cs_2AgSbBr_6$ solution was mixed with 0.333 mL DMSO to form the 0.3 mol L^{-1} $Cs_2AgBiBr_6$ solution. 12 mm × 12 mm glass substrates were cleaned by ultrasonication in acetone and isopropanol for 15 min sequentially, followed by 10 min O_2 plasma cleaning at 300 W (forward power) in a radio frequency (RF) plasma system. The substrates were subsequently taken into a N_2 glovebox and preheated to 75 °C. Precursor solutions were preheated to 75 °C. To deposit the films, the substrate was placed onto a vacuum-free chuck, and 60 µL solution was immediately dropped onto the substrate, before spinning at 4500 rpm for 45 s. Substrates were then annealed at 250 °C for 5 min. The spin-coating and annealing process were undertaken in the N_2 glovebox.

Thin Film Transistor Device Fabrication: For the transistor fabrication, lithographically patterned Cr/Au source drain electrodes were obtained on Si/SiO_2 substrates. This was followed by introducing the perovskite layer with varied concentration which allowed variation in the perovskite grain size.

Measurement and Characterization: XRD was carried out on films with glass substrates in air at room temperature with a B3 Bruker D8 DAVINCI instrument employing Cu Kα radiation.

SEM images were obtained with LEO 1530 VP instrument. Before taking SEM images, films were sputtered with Au/Pd source for 7 s at 65 mA using the Emitech sputter coater. Film thickness was measured by Dektak profilometry.

The absorbance of the $Cs_2AgBiBr_6$ thin film on glass was measured using a Shimadzu UV-3600 Plus spectrometer. The instrument was calibrated to 0% and 100% reflectance/transmittance prior to measuring the sample. The measurements were taken with an interval of 5 nm.

For transient absorption measurements, the third harmonic of a $Nd:YVO_4$ laser system (Picolo-AOT-MOPA 25, InnoLas) at 355 nm with electronically controlled delay was used as pump. For the probe beam, the output of a Ti:sapphire amplifier system (Spectra Physics Solstice Ace) operating at 1 kHz and generating ≈100 fs pulses was sent into a mechanical delay stage (Thorlabs DDS300-E/M). The ultraviolet–visible broadband probe beam (330–700 nm) was generated by focusing the 800 nm fundamental beam onto a CaF_2 crystal (Eksma Optics, 5 mm) connected to a digital motion controller (Mercury C-863 DC Motor Controller) after passing through the mechanical delay stage. The transmitted pulses were collected with a monochrome line scan camera (JAI SW-4000M-PMCL, spectrograph: Andor Shamrock SR-163) with collected data fed straight into the computer.

CL measurements were performed in an Attolight Allalin 4027 Chronos SEM-CL system at RT. Measurements were taken using a beam current of 500 pA and an acceleration voltage of 3 kV which corresponds to 90% of the beam energy being deposited in a depth of 67 nm according to simulations using Monte Carlo Casino software (Figure S3, Supporting Information).[35] The CL hyperspectral maps were analyzed using Hyperspy.

TFT Device Characterization: All the devices were characterized using an Agilent 4155B parameter analyzer operated in pulsed mode. In the pulsed mode of operation, for the transfer (output) measurement, V_g (V_d) was applied over a short impulse of 0.5 ms. The temperature-dependent transport measurements were performed using a Desert Cryogenics low-temperature probe station.

Impedance Spectroscopy: For the impedance measurement, vertical sandwich devices were fabricated with patterned ITO/Au bottom electrode and shadow mask-patterned top Au electrode. Perovskite films were introduced using similar technique as used for FET fabrication. Impedance measurement was performed using Keithley 4200 SCS with a AC voltage of 10 mV while the frequency was varied from 1 kHz to 10 MHz.

In the transient current measurements, a pulse voltage generated by a function generator (Hewlett Packard 8116A) was applied to the hole-only device ($ITO/NiO_x/Cs_2AgBiBr_6/PTAA/Au$). The device was connected in series with a resistor (300 Ω). The voltage across the resistor was measured with an oscilloscope (RS PRO RSDS1304CFL) to monitor the current density kinetics. The samples were mounted in a Desert TTP4 Probe Station for temperature-dependent studies in the range of 230–300 K. The samples were cooled using liquid nitrogen while kept under a vacuum of 10^{-6} mbar.

Supporting Information

Supporting Information is available from the Wiley Online Library or from the author.

Acknowledgements

Z.L. and S.P.S. contributed equally to this work. Z.L. and L.D. would like to thank Cambridge Trust and Chinese Scholarship Council for financial support. R.L.Z.H. acknowledges funding from the Royal Academy of Engineering under the Research Fellowships scheme (No. RF\201718\1701). S.P.S. acknowledged funding support from Royal Society through the Newton Alumni Fellowship, SERB-SRG/2020/001641 and DAE funding through NISER. D.P. acknowledges funding from Peridot Technologies, India. G.K. and R.A.O. acknowledge funding from the EPSRC under Grant No. EP/R025193/1 and thank Dr. Christian Monachon of Attolight for his ongoing support and development of the system. R.S and R.H.F acknowledge funding and support from the SUNRISE project (EP/P032591/1). R.S. acknowledges a Newton International Fellowship from The Royal Society. Y.-T.H. acknowledges funding from the Ministry of Education in the Taiwan Government as well as Downing College Cambridge.

Conflict of Interest

The authors declare no conflict of interest.

Data Availability Statement

The data that support the findings of this study are openly available in Imperial's Data Repository at http://doi.org/10.14469/hpc/8748.

Keywords

carrier mobilities, grain boundaries, ion migration, lead-free double perovskites, thin film transistors

Received: May 25, 2021
Revised: August 6, 2021
Published online: September 4, 2021

© 2021 The Authors. Advanced Functional Materials published by Wiley-VCH GmbH

[1] C. N. Savory, A. Walsh, D. O. Scanlon, *ACS Energy Lett.* **2016**, *1*, 949.
[2] G. Volonakis, M. R. Filip, A. A. Haghighirad, N. Sakai, B. Wenger, H. J. Snaith, F. Giustino, *J. Phys. Chem. Lett.* **2016**, *7*, 1254.
[3] E. T. McClure, M. R. Ball, W. Windl, P. M. Woodward, *Chem. Mater.* **2016**, *28*, 1348.
[4] A. H. Slavney, T. Hu, A. M. Lindenberg, H. I. Karunadasa, *J. Am. Chem. Soc.* **2016**, *138*, 2138.
[5] F. Wei, Z. Deng, S. Sun, F. Zhang, D. M. Evans, G. Kieslich, S. Tominaka, M. A. Carpenter, J. Zhang, P. D. Bristowe, A. K. Cheetham, *Chem. Mater.* **2017**, *29*, 1089.
[6] F. Wei, Z. Deng, S. Sun, F. Xie, G. Kieslich, D. M. Evans, M. A. Carpenter, P. Bristowe, T. Cheetham, *Mater. Horiz.* **2016**, *3*, 328.
[7] F. Wei, Z. Deng, S. Sun, N. T. P. Hartono, H. L. Seng, T. Buonassisi, P. D. Bristowe, A. K. Cheetham, *Chem. Commun.* **2019**, *55*, 3721.
[8] R. L. Z. Hoye, L. Eyre, F. Wei, F. Brivio, A. Sadhanala, S. Sun, W. Li, K. H. L. Zhang, J. L. MacManus-Driscoll, P. D. Bristowe, R. H. Friend, A. K. Cheetham, F. Deschler, *Adv. Mater. Interfaces* **2018**, *5*, 1800464.
[9] F. Igbari, R. Wang, Z. K. Wang, X. J. Ma, Q. Wang, K. L. Wang, Y. Zhang, L. S. Liao, Y. Yang, *Nano Lett.* **2019**, *19*, 2066.
[10] X. Yang, Y. Chen, P. Liu, H. Xiang, W. Wang, R. Ran, W. Zhou, Z. Shao, *Adv. Funct. Mater.* **2020**, *30*, 2001557.
[11] W. Pan, H. Wu, J. Luo, Z. Deng, C. Ge, C. Chen, X. Jiang, W. J. Yin, G. Niu, L. Zhu, L. Yin, Y. Zhou, Q. Xie, X. Ke, M. Sui, J. Tang, *Nat. Photonics* **2017**, *11*, 726.
[12] Z. Zhang, Y. Liang, H. Huang, X. Liu, Q. Li, L. Chen, D. Xu, *Angew. Chem., Int. Ed.* **2019**, *58*, 7263.
[13] D. Bartesaghi, A. H. Slavney, M. C. Gélvez-Rueda, B. A. Connor, F. C. Grozema, H. I. Karunadasa, T. J. Savenije, *J. Phys. Chem. C* **2018**, *122*, 4809.
[14] E. M. Hutter, M. C. Gélvez-Rueda, D. Bartesaghi, F. C. Grozema, T. J. Savenije, *ACS Omega* **2018**, *3*, 11655.
[15] L. Schade, A. D. Wright, R. D. Johnson, M. Dollmann, B. Wenger, P. K. Nayak, D. Prabhakaran, L. M. Herz, R. Nicholas, H. J. Snaith, P. G. Radaelli, *ACS Energy Lett.* **2019**, *4*, 299.
[16] S. J. Zelewski, J. M. Urban, A. Surrente, D. K. Maude, A. Kuc, L. Schade, R. D. Johnson, M. Dollmann, P. K. Nayak, H. J. Snaith, P. Radaelli, R. Kudrawiec, R. J. Nicholas, P. Plochocka, M. Baranowski, *J. Mater. Chem. C* **2019**, *7*, 8350.
[17] E. Greul, M. L. Petrus, A. Binek, P. Docampo, T. Bein, *J. Mater. Chem. A* **2017**, *5*, 19972.
[18] M. Wang, P. Zeng, S. Bai, J. Gu, F. Li, Z. Yang, M. Liu, *Sol. RRL* **2018**, *2*, 1800217.
[19] G. Longo, S. Mahesh, L. R. V. Buizza, A. D. Wright, A. J. Ramadan, M. Abdi-Jalebi, P. K. Nayak, L. M. Herz, H. J. Snaith, *ACS Energy Lett.* **2020**, *5*, 2200.
[20] M. Delor, A. H. Slavney, N. R. Wolf, M. R. Filip, J. B. Neaton, H. I. Karunadasa, N. S. Ginsberg, *ACS Energy Lett.* **2020**, *5*, 1337.
[21] I. Visoly-Fisher, S. R. Cohen, K. Gartsman, A. Ruzin, D. Cahen, *Adv. Funct. Mater.* **2006**, *16*, 649.
[22] M. S. Leite, M. Abashin, H. J. Lezec, A. G. Gianfrancesco, A. A. Talin, N. B. Zhitenev, *IEEE J. Photovolt.* **2014**, *4*, 311.
[23] NREL, Best Research-Cell Efficiency Chart, https://www.nrel.gov/pv/cell-efficiency.html (accessed: June **2021**).
[24] K. Durose, S. E. Asher, W. Jaegermann, D. Levi, B. E. McCandless, W. Metzger, H. Moutinho, P. D. Paulson, C. L. Perkins, J. R. Sites, G. Teeter, M. Terheggen, *Prog. Photovolt. Res. Appl.* **2004**, *12*, 177.
[25] K. L. Chopra, P. D. Paulson, V. Dutta, *Prog. Photovolt. Res. Appl.* **2004**, *12*, 69.
[26] J. Moseley, M. M. Al-Jassim, D. Kuciauskas, H. R. Moutinho, N. Paudel, H. L. Guthrey, Y. Yan, W. K. Metzger, R. K. Ahrenkiel, *IEEE J. Photovolt.* **2014**, *4*, 1671.
[27] N. Nicoara, R. Manaligod, P. Jackson, D. Hariskos, W. Witte, G. Sozzi, R. Menozzi, S. Sadewasser, *Nat. Commun.* **2019**, *10*, 3980.
[28] Z. Li, S. R. Kavanagh, M. Napari, R. Palgrave, M. Abdi-Jalebi, Z. Andaji-Garmaroudi, D. Davies, M. Laitinen, J. Julin, M. A. Isaacs, R. Friend, D. O. Scanlon, A. Walsh, R. L. Z. Hoye, *J. Mater. Chem. A* **2020**, *8*, 21780.
[29] W. A. Dunlap-Shohl, Y. Zhou, N. P. Padture, D. B. Mitzi, *Chem. Rev.* **2019**, *119*, 3193.
[30] J. A. Steele, P. Puech, M. Keshavarz, R. Yang, S. Banerjee, E. Debroye, C. W. Kim, H. Yuan, N. H. Heo, J. Vanacken, A. Walsh, J. Hofkens, M. B. J. Roeffaers, *ACS Nano* **2018**, *12*, 8081.
[31] R. Kentsch, M. Scholz, J. Horn, D. Schlettwein, K. Oum, T. Lenzer, *J. Phys. Chem. C* **2018**, *122*, 25940.
[32] R.-I. Biega, M. R. Filip, L. Leppert, J. B. Neaton, *J. Phys. Chem. Lett.* **2021**, *12*, 2057.
[33] B. Wu, W. Ning, Q. Xu, M. Manjappa, M. Feng, S. Ye, J. Fu, S. Lie, T. Yin, F. Wang, T. W. Goh, P. C. Harikesh, Y. K. E. Tay, Z. X. Shen, F. Huang, R. Singh, G. Zhou, F. Gao, T. C. Sum, *Sci. Adv.* **2021**, *7*, eabd3160.
[34] E. V. Peán, S. Dimitrov, C. S. De Castro, M. L. Davies, *Phys. Chem. Chem. Phys.* **2020**, *22*, 28345.
[35] D. Drouin, A. R. Couture, D. Joly, X. Tastet, V. Aimez, R. Gauvin, *Scanning* **2007**, *29*, 92.
[36] H. Guthrey, J. Moseley, *Adv. Energy Mater.* **2020**, *10*, 1903840.
[37] F. de la Peña, V. T. Fauske, P. Burdet, E. Prestat, P. Jokubauskas, M. Nord, T. Ostasevicius, K. E. MacArthur, M. Sarahan, *hyperspy/hyperspy v1.4.1*, **2018**, https://zenodo.org/record/1469364#.YQ0euS1Q1do (accessed: July 2021).
[38] S. Groudeva-Zotova, W. Jacob, A. Von Keudell, *Diamond Relat. Mater.* **1996**, *5*, 1087.
[39] N. Zhang, M. Cao, W. Z. Cui, T. C. Hu, *Jpn. J. Appl. Phys.* **2017**, *56*, 075802.
[40] E. Fortunato, P. Barquinha, R. Martins, *Adv. Mater.* **2012**, *24*, 2945.
[41] J. Wang, S. P. Senanayak, J. Liu, Y. Hu, Y. Shi, Z. Li, C. Zhang, B. Yang, L. Jiang, D. Di, A. V. Ievlev, O. S. Ovchinnikova, T. Ding, H. Deng, L. Tang, Y. Guo, J. Wang, K. Xiao, D. Venkateshvaran, L. Jiang, D. Zhu, H. Sirringhaus, *Adv. Mater.* **2019**, *31*, 1902618.
[42] S. P. Senanayak, B. Yang, T. H. Thomas, N. Giesbrecht, W. Huang, E. Gann, B. Nair, K. Goedel, S. Guha, X. Moya, C. R. McNeill, P. Docampo, A. Sadhanala, R. H. Friend, H. Sirringhaus, *Sci. Adv.* **2017**, *3*, e1601935.
[43] N. Karl, *Synth. Met.* **2003**, *133*, 649.
[44] E. Bandiello, J. Ávila, L. Gil-Escrig, E. Tekelenburg, M. Sessolo, H. J. Bolink, *J. Mater. Chem. A* **2016**, *4*, 18614.
[45] H. Zhang, H. Lin, C. Liang, H. Liu, J. Liang, Y. Zhao, W. Zhang, M. Sun, W. Xiao, H. Li, S. Polizzi, D. Li, F. Zhang, Z. He, W. C. H. Choy, *Adv. Funct. Mater.* **2015**, *25*, 7226.
[46] Q. Dong, J. Mendes, L. Lei, D. Seyitliyev, L. Zhu, S. He, K. Gundogdu, F. So, *ACS Appl. Mater. Interfaces* **2020**, *12*, 48845.
[47] Z. Xiao, W. Meng, J. Wang, Y. Yan, *ChemSusChem* **2016**, *9*, 2628.
[48] M. H. Futscher, M. K. Gangishetty, D. N. Congreve, B. Ehrler, *J. Chem. Phys.* **2020**, *152*, 044202.
[49] L. McGovern, I. Koschany, G. Grimaldi, L. A. Muscarella, B. Ehrler, *J. Phys. Chem. Lett.* **2021**, *12*, 2423.
[50] Y. Yin, W. Tian, J. Leng, J. Bian, S. Jin, *J. Phys. Chem. Lett.* **2020**, *11*, 6956.
[51] B. G. Horowitz, *Adv. Mater.* **1998**, *10*, 365.
[52] G. Horowitz, M. E. Hajlaoui, R. Hajlaoui, *J. Appl. Phys.* **2000**, *87*, 4456.
[53] M. D. Smith, H. I. Karunadasa, *Acc. Chem. Res.* **2018**, *51*, 619.
[54] M. Swift, A. Janotti, C. G. Van De Walle, *Phys. Rev. B* **2015**, *92*, 214114.

© 2021 The Authors. Advanced Functional Materials published by Wiley-VCH GmbH